Phys Chem Minerals (2011) 38:397–406
DOI 10.1007/s00269-010-0413-0

ORIGINAL PAPER

Synthetic lead bromapatite: X-ray structure at ambient pressure and compressibility up to about 20 GPa

Xi Liu · Michael E. Fleet · Sean R. Shieh · Qiang He

Received: 13 October 2010 / Accepted: 2 December 2010 / Published online: 23 December 2010

Abstract Lead bromapatite [$Pb_{10}(PO_4)_6Br_2$] has been synthesized via solid-state reaction at pressures up to 1.0 GPa, and its structure determined by single-crystal X-ray diffraction at ambient temperature and pressure. The large bromide anion is accommodated in the *c*-axis channel by lateral displacements of structural elements, particularly of Pb2 cations and PO_4 tetrahedra. The compressibility of bromapatite was also investigated up to about 20.7 GPa at ambient temperature, using a diamond-anvil cell and synchrotron X-ray radiation. The compressibility of lead bromapatite is significantly different from that of lead fluorapatite. The pressure–volume data of lead bromapatite ($P < 10$ GPa) fitted to the third-order Birch-Murnaghan equation yield an isothermal bulk modulus (K_T) of 49.8(16) GPa and first pressure derivative (K_T') of 10.1(10). If K_T' is fixed at 4, the derived K_T is 60.8(11) GPa. The relative difference of the bulk moduli of these two lead apatites is thus about 12%, which is about two times the relative difference of the bulk moduli ($\sim$5%) of the calcium apatites fluorapatite [$Ca_{10}(PO_4)_6F_2$], chlorapatite [$Ca_{10}(PO_4)_6Cl_2$] and hydroxylapatite [$Ca_{10}(PO_4)_6(OH)_2$]. Another interesting feature apparently related to the replacement of F by Br in lead apatite is the switch in the principle axes of the strain ellipsoid: the *c*-axis is less compressible than the *a*-axis in lead bromapatite but more compressible in lead fluorapatite.

Keywords Lead bromapatite · Solid-state synthesis · Crystal structure · Compressibility · Synchrotron powder X-ray diffraction · Environment

Introduction

Apatite compounds have the structural formula $M1_2M2_3(BO_4)_3X$, where M1 and M2 are large cations [primarily Na^+, Ag^+, Ca^{2+}, Sr^{2+}, Ba^{2+}, Cd^{2+}, Pb^{2+}, and rare-earth elements (REE^{3+})], B metalloids (P^{5+}, C^{3+}, S^{6+}, Si^{4+}, As^{5+}, and V^{5+}), and X halides or oxy-anions [$(OH)^-$, F^-, Cl^-, Br^-, I^-, $(CO_3)^{2-}$, $(HCO_3)^-$, O^{2-}, H_2O and other small neutral molecules, and vacancies] (Kim et al. 2000; Pan and Fleet 2002; White and Dong 2003; White et al. 2005; Fleet and Liu 2007a). The mineralogy and geochemistry of the calcium apatites (mainly hydroxylapatite, fluorapatite and francolite, and chlorapatite) have been extensively investigated because of their importance in various types of rocks, biomineralization and the environment, and agriculture (e.g. Ma et al. 1993; Hughes and Rakovan 2002; Fleet and Liu 2007a, b, 2008a, b; Fleet 2009; Filiberto and Treiman 2009). Lead apatites have also gained much attention recently since Suzuki et al. (1984) reported the extensive cation exchange of Ca^{2+} in hydroxylapatite by Pb^{2+} cations in aqueous solution at low pH and room temperature; this means that hydroxylapatite can be used to effectively remediate the lead contamination of soil (Ma et al. 1993). In addition, pyromorphite

Electronic supplementary material The online version of this article (doi:10.1007/s00269-010-0413-0) contains supplementary material, which is available to authorized users.

X. Liu (✉) · Q. He
Key Laboratory of Orogenic Belts and Crustal Evolution, MOE, Peking University, 100871 Beijing, People's Republic of China
e-mail: xi.liu@pku.edu.cn

X. Liu · Q. He
School of Earth and Space Sciences, Peking University, 100871 Beijing, People's Republic of China

X. Liu · M. E. Fleet · S. R. Shieh
Department of Earth Sciences, University of Western Ontario, London, ON N6A 5B7, Canada

(lead chlorapatite) is associated with the final step of the lead cycle in roadside ecosystems (Nriagu 1984), and more recently lead hydroxylapatite has been identified as a corrosion product of lead pipes in a municipal water supply (Peters et al. 1999).

Although calcium bromapatite can be found in some astral bodies such as meteorites (Lodders and Fegley 1998), it does not occur naturally on Earth. In fact, the Br content in terrestrial apatites is generally less than 100 ppm (Walters and Luth 1969; O'Reilly and Griffin 2000; Pan and Dong 2003), so that the geological role of calcium bromapatite is not important, and all previous investigations have been focused on its crystal chemistry, thermodynamic properties, and electronic structure and bonding (Dykes 1974; Condrate et al. 1975; Elliott et al. 1981; Kim et al. 2000; Rulis et al. 2004; Boujrhal et al. 2004; Cruz et al. 2005a, b). Lead bromapatite has not been reported as a mineral, and scientific interest has been limited to crystal chemical and environmental aspects (Bhatnaga 1971; Nriagu 1973; Kim et al. 2000; Kaluderovic et al. 2001). In the present paper, we investigate the synthesis, *P–T* stability field, crystal structure and compressional behaviour of lead bromapatite.

Experimental details

Lead bromapatite was synthesized via solid-state reaction variously in a conventional muffle furnace at one atm, a standard cold-seal hydrothermal reaction vessel at 2.1 kbar, and a piston-cylinder apparatus at 10 kbar (Depths of the Earth Company Quickpress). The starting material was a mechanical stoichiometric mixture of reagent-grade lead bromide ($PbBr_2$) and lead orthophosphate [$Pb_3(PO_4)_2$], which was homogenized and encapsulated in a sealed noble metal tube (Pt or Au): see Liu and Fleet (2009) for the high-*P* experimental techniques.

The products from the synthesis experiments were examined by optical microscopy, powder X-ray diffraction (Rigaku D/MAX-B system; Co $K\alpha$ X-radiation; Department of Earth Sciences, University of Western Ontario), Fourier transform infrared spectroscopy (FTIR; Nicolet Nexus 670 FTIR spectrometer; Department of Earth Sciences, University of Western Ontario), and electron probe micro-analysis (EPMA; JEOL JXA-8100; School of Earth and Space Sciences, Peking University (PKU)). In addition, one prismatic crystal from the product LM183 (Table 1) was characterized by single-crystal X-ray structure study (Bruker-Nonius Kappa CCD diffractometer and graphite-monochromatized Mo $K\alpha$ X-radiation; 50 kV, 32 mA, $\lambda = 0.7107$ Å; Department of Chemistry, University of Western Ontario).

Single crystal X-ray diffraction measurements were made at room temperature and pressure. The COLLECT software (Bruker-Nonius 1997) was used for unit-cell refinement and data collection. The reflection data were processed with SORTAV-COLLECT, using an empirical procedure for absorption correction. Structure refinement was made with LINEX77 (Coppens 1977). Scattering factors for neutral atomic species and values of the anomalous scattering factors f' and f'' were taken, respectively, from Tables 2.2A and 2.3.1 of the International Tables for X-ray Crystallography (Ibers and Hamilton 1974).

Compression experiments were conducted using a symmetrical diamond-anvil cell and angle dispersive X-ray diffraction technique up to about 20.7 GPa at the beamline X17C, National Synchrotron Light Source, Brookhaven National Laboratory. In general the experimental techniques used here were very similar to those reported by Liu et al. (2008). T301 stainless steel plates with an initial thickness of 250 μm were used as gaskets. The central area of the plates was pre-indented to a thickness of about 30 μm, and a hole of 150 μm in diameter was subsequently eroded electrically. The lead bromapatite powder (LM180; Table 1), along with two small ruby balls, was loaded with the pressure medium (a 4:1 methanol–ethanol mixture which was expected to solidify at about 10 GPa at 300 K) into the hole in the gasket. With the ruby fluorescence method (Mao et al. 1978), the experimental pressure was measured before and after each X-ray analysis. The incident synchrotron radiation beam was monochromatized to a wavelength of 0.4066 Å, and the beam size was collimated to a diameter of $\sim 25 \times 20$ μm^2. The X-ray diffraction pattern of the sample at each pressure interval was collected with an exposure time of 10 min using an online CCD detector, and later integrated as a function of 2θ to give the conventional one-dimensional X-ray profile using the Fit2D program (Hammersley 1996). The unit-cell

Table 1 Synthesis experiments and observations

Run #	Apparatus	*P* (kbar)	*T* (°C)	Time (h)	Phase observed
LM180	MF	0.001	500	22	Apatite
LM181	MF	0.001	800	22	Apatite, unknown phase[a]
LM183[b]	MF	0.001	900/750	20/87	Apatite, unknown phase[a]
LM185	MF	0.001	1,000	20	Apatite, melt
LM184	HR	2.1	800	72	Apatite, unknown phase[a]
LM190	PC	10	1,000	8	Apatite

MF muffle furnace, *HR* hydrothermal reaction line, *PC* piston-cylinder apparatus

[a] The unknown phase is potentially a monoclinic lead orthophosphate as suggested by the powder X-ray diffraction data and the EPMA analyses

[b] Experimental temperature was 900°C for 20 h, decreased to 750°C by 0.05°C/min, and then 750°C for 87 h

parameters of lead bromapatite were then calculated by refining the unit cell using the positions of the strongest diffraction peaks, such as 110, 200, 111, 102, 210, 211, 112, 300, 113, 222, 312, 123, 321, 410, 402, and 004.

Results and discussion

Experimental details of the synthesis experiments are summarized in Table 1. A selection of electron back-scatter images and powder X-ray diffraction patterns of the products are presented in Fig. 1 and SI-Fig. 1 (see Supplementary Information), respectively. Details and results of the single-crystal X-ray diffraction investigation are given in Fig. 2 and Tables 2, 3, 4 and 5 and SI-Table 1 (see Supplementary Information). Typical powder X-ray diffraction patterns collected in situ in the compression experiments are shown in Fig. 3, and the unit-cell parameters of lead bromapatite derived from the synchrotron X-ray radiation data are summarized in Table 6.

Composition and phase relations

Six synthesis experiments were conducted under various *P–T* conditions (Table 1), and all yielded lead bromapatite. The products from LM180 and LM190 were nearly pure lead bromapatite while those from other experiments consisted of lead bromapatite with subordinate amounts of a second phase (the mid-gray phase in the BSI images in Fig. 1a, b), which was tentatively identified as metal-deficient monoclinic lead orthophosphate, based on powder X-ray diffraction (see SI-Fig. 1 in the Supplementary Information) and EPMA. The proportion of this second phase increased with increase in temperature and was greatest for experiments at high temperature and room pressure (experiment LM185; Table 1, SI-Fig. 1). Therefore, we attribute the presence of this phase to leakage of $PbBr_2$ from the sample capsules. The EPMA analyses indicated that the synthetic lead bromapatite was essentially stoichiometric but the lead orthophosphate was non-stoichiometric, and presumably partially oxidized. For LM183, the experiment used for the single-crystal X-ray structure, the PKU EPMA data suggested a formulae of $Pb_{9.9}(PO_4)_6Br_{2.1}$ for lead bromapatite and $Pb_{2.5}(PO_4)_2$ for the lead orthophosphate. The result for the lead bromapatite is supported by site occupancy refinements from the single-crystal study, which gave occupancies of 0.97, 1.03 and 0.97 for Pb1, Pb2 and Br sites, respectively. Furthermore, the single-crystal unit-cell parameters of $a = 10.0622(1)$ and $c = 7.3575(3)$ Å are closely comparable to those of LM180 ($a = 10.063(1)$ and $c = 7.367(1)$ Å), the material that was used for the compression studies at ambient temperature. In summary, lead bromapatite appeared to be stable over the range of

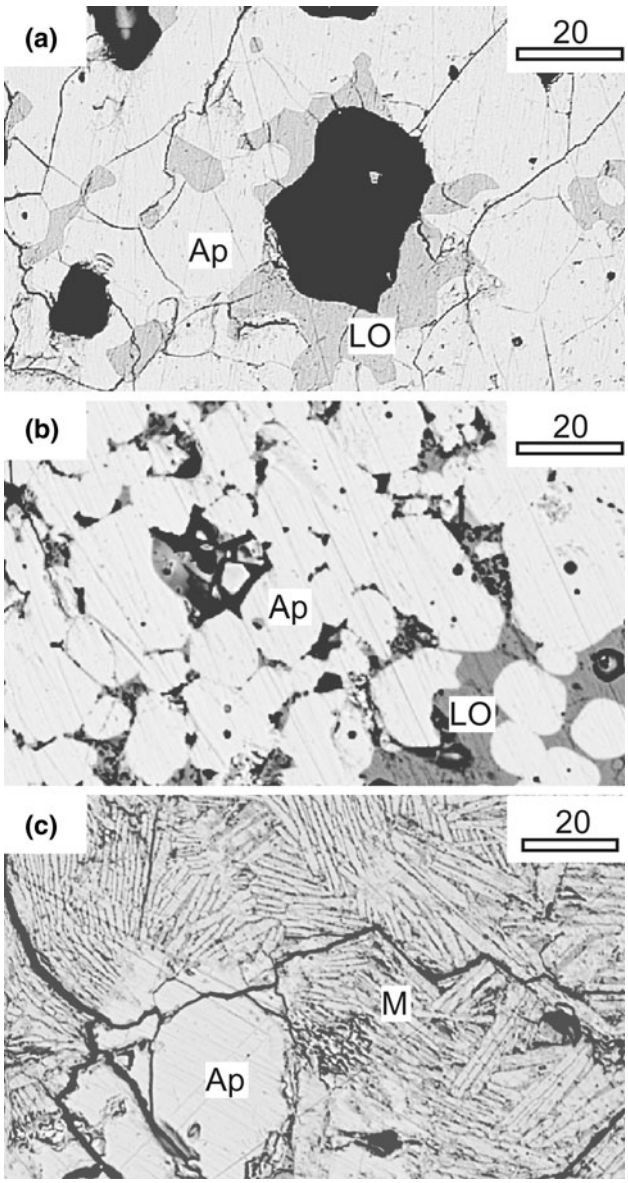

Fig. 1 Electron back-scatter images showing the textures of synthesized materials in **a** LM183, **b** LM184 and **c** LM185. Lead bromapatite (Ap *bright*) coexists with minor lead orthophosphate (LO *mid gray*) in **a** and **b** and quenched melts (M) showing dendritic texture in **c**. *Scale bars* are 20 μm

P–T conditions covered by the synthesis experiments. With the actual melting reaction unknown, the melting point of lead bromapatite at ambient pressure seems to be close to 900°C, as bracketed by the experiments LM181 and LM185 (Table 1), which is much lower than the melting point of lead fluorapatite (about 1,098°C; Podsiadlo 1990).

Crystal structure of lead bromapatite at room temperature and pressure

The stoichiometric composition $Pb_{10}(PO_4)_6Br_2$ was assumed for the single-crystal structure analysis of lead

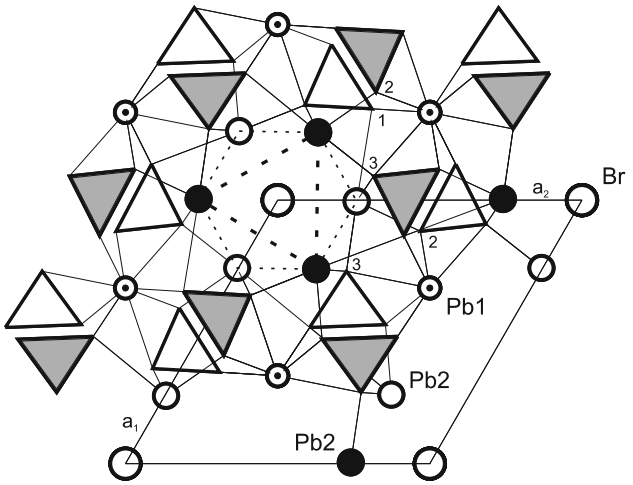

Fig. 2 Structure of lead bromapatite identifying channel polyhedron (*broken lines*) formed by Pb2 cations in apatite channel wall: *open* Pb2 *circles* are at height $z = 1/4$ and *closed circles* are at $z = 3/4$; *triangles* are PO_4 tetrahedra centered at $z = 1/4$ (*open*) and $z = 3/4$ (*shaded*); numbers (1, 2, 3) identify oxygen atoms forming corners of tetrahedra

Table 2 Experimental details for single-crystal X-ray structure

Experiment	LM183
Crystal	xt403
Crystal size (mm)	0.06 × 0.06 × 0.08
Crystal shape	Prism
a (Å)	10.0622(5)[a]
c (Å)	7.3575(3)
Space group	$P6_3/m$
Formula weight	2801.54
Density (g/cm^3)	7.211
Reflections—unique	683
($I < 3\sigma_{(I)}$)	253
$R_{(I)}$	0.068
$R_{(I),w}$	0.045
Refined parameters	40
μ (cm^{-1})	685.5
R	0.042
Rw	0.040
s	1.37
g (× 10^4)	0.26(1)
$\Delta\rho$ (eÅ^{-3})	
(+)	2.6
(−)	3.2

[a] Number in parentheses represents one standard deviation in the rightmost digit

bromapatite at room temperature and pressure. The results for refinement of the apatite type structure are summarized in Tables 2 (experimental details) and 3 (positional and thermal/displacement parameters) and Fig. 2. In the apatite structure, isolated PO_4 tetrahedra centered at $z = 1/4,3/4$ are linked by Pb1 in ninefold (6 + 3) coordination and Pb2 in an irregular sevenfold (6 + 1) coordination. A prominent feature is the large c-axis channel which is defined by triclusters of M2 cations at $z = 1/4,3/4$ (Fig. 2) and accommodates a variety of X anion components. The local coordination of the channel anion varies considerably with size and complexity of the anion (Hughes et al. 1989; Fleet and Liu 2007b) and size of the M2 cations (e.g. Fleet et al. 2010). In calcium fluorapatite, the F anion is located on the c-axis at $z = 1/4,3/4$ in the center of a tricluster of Ca2 cations. However, in apatites with large divalent M2 cations the channel anion is displaced along the c-axis towards $z = 1/2$, occupying a split atom position with occupancy of 0.5 (Bigi et al. 1989; Kim et al. 2000; Badraoui et al. 2001, 2006); e.g. in strontium-lead fluorapatite solid solutions, the z coordinate of fluorine increases progressively with increasing content of lead from near 0.25 in strontium fluorapatite to near 0.5 in lead fluorapatite (Badraoui et al. 2006). Following this trend, the bromine anion is displaced to $z = 0.487$ in the channel of lead bromapatite (Table 3) and the fluorine anion to $z = 0.461$ in the channel of lead fluorapatite (Fleet et al. 2010). The channel bromide/fluoride anion in these two structures has six nearest-neighbor Pb2 cations in the channel wall, in the approximate configuration of a trigonally-distorted octahedron (Fig. 2). Note that the displacement of the X anion away from $z = 1/4$ is greater for the bromapatite due to the larger size of the Br^- anion.

Table 3 Positional and isotropic thermal parameters (Å^2) from single crystal study $U_{eq} = (1/3)\sum_i\sum_j U^{ij}\, a^i a^j\, a_i.a_j$

	Site occupancy	x	y	z	U (U_{eq})
Pb1	1.0	2/3	1/3	0.0055(1)[a]	0.0184(5)
Pb2	1.0	0.00452(8)	0.26188(8)	0.25	0.0192(3)
P	1.0	0.3771(6)	0.4113(5)	0.25	0.007(1)
O1	1.0	0.483(1)	0.347(1)	0.25	0.014(3)
O2	1.0	0.472(1)	0.590(1)	0.25	0.013(3)
O3	1.0	0.270(1)	0.361(1)	0.084(1)	0.024(3)
Br	0.5	0	0	0.487(2)	0.019(1)

[a] Number in parentheses represents one standard deviation in the rightmost digit

Table 4 summarizes results for refinements of the structures of lead bromapatite and lead fluorapatite (Fleet et al. 2010) with the X anion located in the three axial positions permitted by space group $P6_3/m$. In each case, the split atom position (equipoint 4*e*; refinements 1 and 4) results in the most acceptable structure, based on reduction of residual indices (R, Rw) and goodness-of fit closest to unity, as well as most reasonable isotropic displacement parameter. Refinement of lead fluorapatite with $z = 1/4$

Table 4 Refinement of channel (X) anion in space group $P6_3/m$

Refinement	Equipoint	Site occupancy	X position			U (Å^2)	R	Rw	s
			x	y	z				
Lead bromapatite									
1	4*e*	0.5	0	0	0.487(2)	0.019(1)	0.042	0.040	1.37
2	2*b*	1.0	0	0	1/2	0.0224(9)	0.043	0.041	1.39
3	2*a*	1.0	0	0	1/4	0.073(9)	0.148	0.205	6.90
Lead fluorapatite[a]									
4	4*e*	0.5	0	0	0.461(4)	0.030(9)	0.043	0.034	1.01
5	2*b*	1.0	0	0	1/2	0.063(8)	0.043	0.035	1.03
6	2*a*	1.0	0	0	1/4	0.025[b]	0.057	0.064	1.87

Only results for X anion position are shown for each refinement. U is isotropic displacement, R, Rw and s are residual index, weighted residual index and goodness-of-fit, respectively

[a] Results for refinement of lead fluorapatite with split atom position (equipoint 4*e*) are from Fleet et al. (2010). Value of 1.0 for occupancy of fluorine in Table 2 of Fleet et al. (2010) is a typographical error

[b] Not refined

Table 5 Bond distances (Å) and angles (°)

Bond/Angle	PbBrAP[a]	PbFAP[b]	FAP[c]	PbOAP[d]	PbHAP[e]
a (Å)	10.0622(5)[f]	9.7638(6)	9.398(3)	9.8650(3)	9.866(3)
c (Å)	7.3575(3)	7.2866(4)	6.878(2)	7.4306(3)	7.426(2)
Pb1–O1 × 3	2.631(9)	2.51	2.40	2.56	2.67
Pb1–O2^{I} × 3	2.675(9)	2.73	2.46	2.66	2.62
Pb1–O3^{I} × 3	2.89(1)	2.85	2.81	2.94	3.01
Mean	2.73	2.70	2.55	2.72	2.77
Pb2–O1^{II}	3.10(1)	2.93	2.70	2.95	2.89
Pb2–O2^{III}	2.33(1)	2.38	2.37	2.44	2.54
Pb2–O3^{IV} × 2	2.64(1)	2.59	2.35	2.60	2.59
Pb2–O3 ^{V} × 2	2.66(1)	2.64	2.50	2.64	2.62
Mean	2.67	2.63	2.46	2.64	2.64
Pb2–Br[g]	3.139(7)	2.75	2.31	2.58	2.90
Pb2–Br	3.253(8)	3.11	–	–	–
P–O1	1.50(1)	1.53	1.54	1.56	1.51
P–O2	1.54(1)	1.53	1.54	1.57	1.51
P–O3 × 2	1.56(1)	1.54	1.53	1.55	1.51
Mean	1.53	1.53	1.54	1.55	1.51
O1–P–O2	109.9(7)	109.9	111.0	109.4	109.5
O1–P–O3 × 2	112.9(5)	111.0	111.1	111.9	109.5
O2–P–O3 × 2	107.9(5)	109.1	108.0	108.6	109.5
O3–P–O3^{VI}	105.0(8)	106.7	107.4	106.4	109.5

[a] Lead bromapatite, single crystal (this study)

[b] Lead fluorapatite, single crystal (Fleet et al. 2010)

[c] Fluorapatite, single crystal (Hughes et al. 1989)

[d] Lead oxyapatite, single crystal (Krivovichev and Burns 2003)

[e] Lead hydroxyapatite, powder, rigid body PO_4 refinement (Brückner et al. 1995)

[f] Number in parentheses represents one standard deviation in the rightmost digit

[g] Pb2-Br(F,O,OH)

(I) $1 - x$, $1 - y$, $-z$; (II) $1 - y$, $x - y$, z; (III) $1 - x+y$, $1 - x$, z; (IV) $1 + x$, y, z; (V) $1 + x–y$, x, $-z$; (VI) x, y, ½ $- z$

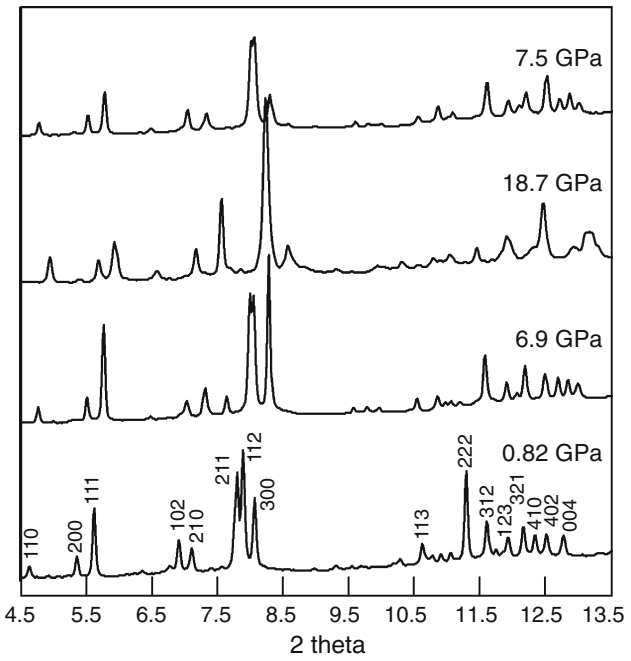

Fig. 3 Examples of X-ray diffraction patterns of lead bromapatite at 0.82, 6.9, 18.7 and 7.5 GPa. The X-ray diffraction patterns at 0.82, 6.9 and 18.7 GPa were collected during compression while the one at 7.5 GPa was collected during decompression. Note the peak-broadening at 18.7 GPa

Table 6 Unit-cell parameters of lead bromapatite at different pressures

P (GPa)	*a* (Å)	*c* (Å)	*V* (Å^3)	*a*/*c*
0.0001	10.063(1)[a]	7.367(1)	646.1(1)	1.3660(2)
0.82(2)	10.013(1)	7.320(1)	635.6(1)	1.3679(2)
1.48(3)	9.969(1)	7.301(1)	628.4(1)	1.3654(2)
3.82(8)	9.863(1)	7.246(1)	610.4(1)	1.3612(2)
4.68(0)	9.822(1)	7.226(1)	603.7(1)	1.3593(2)
5.8(1)	9.776(2)	7.203(2)	596.2(2)	1.3572(5)
6.9(2)	9.742(1)	7.189(1)	590.9(1)	1.3551(2)
7.9(2)	9.704(1)	7.170(1)	584.8(2)	1.3534(2)
8.9(1)	9.672(2)	7.154(2)	579.6(2)	1.3520(5)
10.6(2)	9.619(1)	7.136(1)	571.8(2)	1.3480(2)
12.4(1)	9.587(1)	7.121(1)	566.9(2)	1.3463(2)
14.6(2)	9.542(3)	7.107(3)	560.4(4)	1.3426(7)
16.3(1)	9.495(3)	7.084(3)	553.1(4)	1.3403(7)
18.7(1)	9.413(3)	7.081(4)	543.4(4)	1.3293(9)
20.7(2)	9.332(7)	7.073(4)	533.5(6)	1.319(1)
7.5(2)[b]	9.721(1)	7.182(1)	587.7(1)	1.3535(2)
2.87(2)[b]	9.908(1)	7.265(1)	617.6(1)	1.3638(2)

[a] Number in parentheses represents one standard deviation in the rightmost digit

[b] Data collected during decompression

(refinement 6) did not converge with *U* set as a variable parameter, and the corresponding refinement of lead bromapatite (refinement 3) resulted in unacceptably high values for *U*, *R*, *Rw*, and *s*. Using the weighted residual index (*Rw*) and the theory of Hamilton (1965), the improvement in the 4*e* refinement over that of equipoint 2*b* (refinements 2 and 5) is significant beyond the 99% level for both lead bromapatite and lead fluorapatite. Our conclusion that the X anions are located in equipoint 4*e* and, therefore, disordered in the apatite channel, in both structures, is further supported by their behavior during refinement. We emphasize that the *z* coordinate and isotropic displacement parameters for refinements 1 and 4 in Table 4 were obtained by unconstrained refinement. When these refinements are started with the X anions at $z = 1/2$, the respective *z* coordinates return to their minimized values of 0.487(2) for lead bromapatite and 0.461(4) for lead fluorapatite. This exercise strongly suggests that the single-crystal X-ray reflection intensities represent pairs of closely spaced X anions of half occupancy in the apatite channel, and not one atom of unit occupancy in the special position 2*b* at 0, 0, 1/2.

A selection of bond distances and angles for lead bromapatite is given in Table 5, along with comparison data for lead fluorapatite (Fleet et al. 2010), fluorapatite (Hughes et al. 1989), lead oxyapatite (Krivovichev and Burns 2003), and lead hydroxylapatite (Brückner et al. 1995). Whereas the overall structure of lead fluorapatite was similar to that of fluorapatite except for accommodation of the channel anion (Fleet et al. 2010), there are significant differences between the structures of lead bromapatite and lead fluorapatite. These differences are related to accommodation of the large channel anion in lead bromapatite: the effective ionic radii for sixfold coordination are 1.96 Å for Br and 1.33 Å for F (Shannon 1976). The bromide anion of lead bromapatite is displaced only marginally closer to $z = 1/2$ than the fluoride anion of lead fluorapatite ($z = 0.487$, 0.461, respectively) and has the same trigonally-distorted octahedral coordination. However, the Pb2 cation and PO_4 tetrahedron are shifted laterally, away from the *c*-axis; in particular, the *y* coordinate of Pb2 is 0.2357 for lead fluorapatite but 0.2619 for lead bromapatite, and the Pb2–O1 and short Pb2–Br bonds are increased correspondingly to 3.10 and 3.139 Å, respectively. Note that the Rietveld study of Kim et al. (2000) using combined synchrotron X-ray and neutron powder diffraction data did not yield information on either the oxygen atom positions (O1, O2, and O3) or the precise position of the Br-anion in the channel and, therefore, overlooked important crystal chemical features in the structure of lead bromapatite.

Compressibility of lead bromapatite

At room temperature, lead bromapatite was found to be stable up to at least 20.7 GPa (Fig. 3). The X-ray diffraction patterns at 18.7 and 20.7 GPa show apparent

peak-broadening (see SI-Fig. 2 in Supplementary Information), which might imply the onset of the instability of lead bromapatite; alternatively, the peak-broadening might merely indicate the build-up of stress in the diamond-anvil cell. The pressure medium solidifies at ~10 GPa, so that maintaining a completely hydrostatic condition at higher pressure becomes impractical. Even so, the observed diffraction reflections at 18.7 and 20.7 GPa refine to give a typical lead bromapatite unit-cell (Table 6). As pressure increases from the ambient pressure, all diffraction peaks shift to larger 2θ angles (Fig. 3), indicating the shrinking of the unit cell of lead bromapatite (Table 6). Consequently, some peak-overlap inevitably occurs at high pressure: for instance, peaks 211 and 112 are difficult to separate at pressures above 10 GPa. In addition, the X-ray patterns collected at 7.5 and 2.87 GPa during decompression show that the elastic behaviour of lead bromapatite is fully reversible after compression to 20.7 GPa (Figs. 3, 4, 5, 6).

The room-pressure unit-cell parameters and volume of the present lead bromapatite are $a = 10.063(1)$ Å, $c = 7.367(1)$ Å, and $V = 646.1(1)$ Å^3; these values are closely comparable to the literature data for lead bromapatite [$a = 10.0618(3)$ Å, $c = 7.3592(1)$ Å; Kim et al. 2000]. Since the room-pressure unit-cell parameters and volume of lead fluorapatite are $a = 9.757(3)$ Å, $c = 7.283(4)$ Å, and $V = 600.4(3)$ Å^3 (Liu et al. 2008), replacing F by Br apparently causes both unit-cell parameters and volume of the lead apatite to increase: a is increased by ~ 3%, c by ~1%, and V by ~8%. For the calcium apatites $Ca_{10}(PO_4)_6F_2$ and $Ca_{10}(PO_4)_6Br_2$ (Sudarsanan et al. 1972; Elliott et al. 1981; Kim et al. 2000), however, the changes of the unit-cell parameters and volume caused by the substitution of F by Br are: a to increase by ~4%, c to decrease by ~2% and V to increase by ~6%.

The effect of pressure on the unit-cell parameters and volume of lead bromapatite at room temperature is summarized in Table 6 and graphically shown in Figs. 4, 5 and 6.

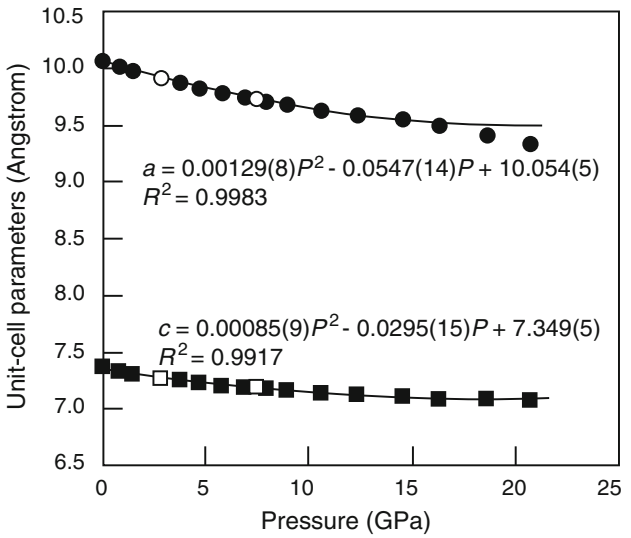

Fig. 4 Pressure dependence of the unit-cell parameters a and c of lead bromapatite at 300 K. *Filled symbols* are for data collected during compression *while empty symbols* for data collected during decompression. Note that for most data points their *error bars* are smaller than the *symbols*. Equations are empirically regressed from the data below 18 GPa

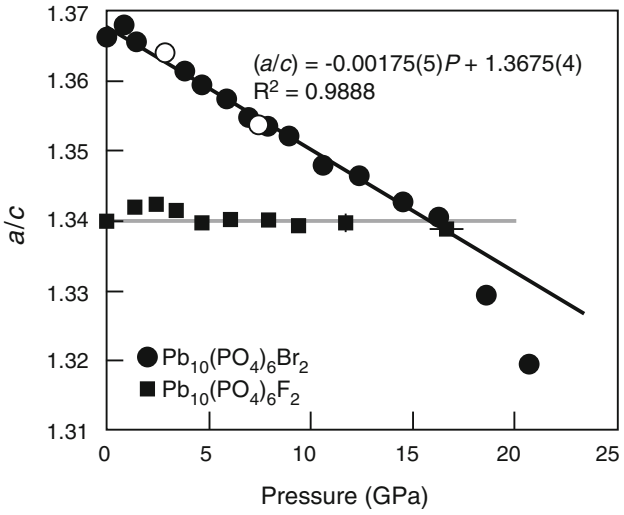

Fig. 5 Variation in a/c of lead bromapatite with increase in pressure, compared to lead fluorapatite. While the a/c ratio of lead flourapatite is generally constant for the experimentally-covered P interval, that of lead bromapatite is apparently not. *Filled symbols* are for data collected during compression while *empty symbols* for data collected during decompression. Equation is empirically regressed from the data below 18 GPa. Data for lead fluoapatite are from Liu et al. (2008)

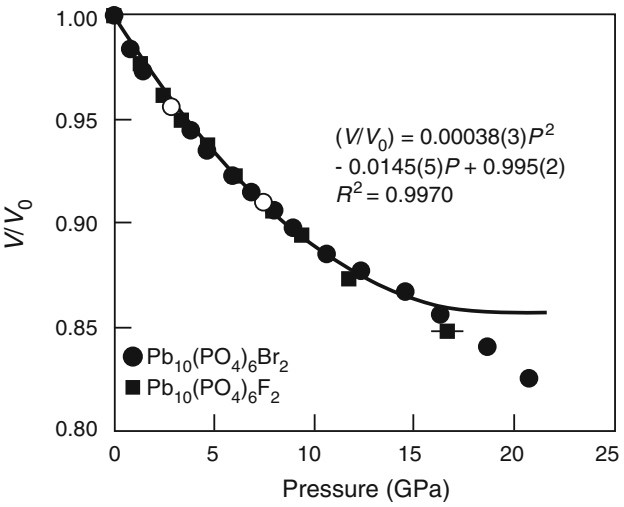

Fig. 6 Pressure-volume data of lead bromapatite at 300 K, compared to lead fluorapatite. *Filled symbols* are for data collected during compression while *empty symbols* for data collected during decompression. Equation is empirically regressed from the data below 18 GPa

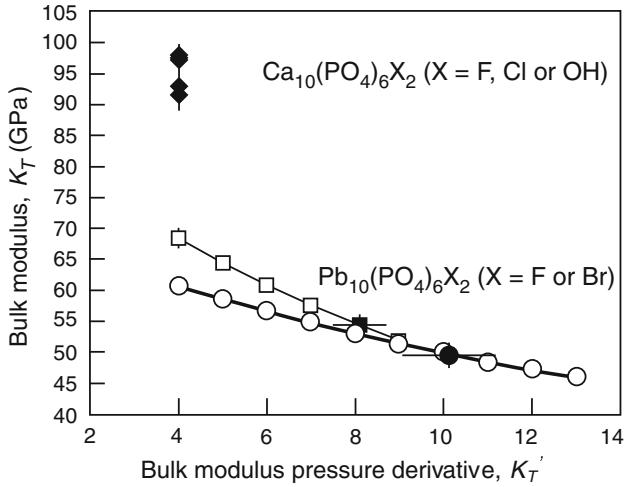

Fig. 7 Comparison of the isothermal bulk moduli of lead bromapatite with lead fluorapatite and calcium hydroxylapatite-fluorapatite-chlorapatite at 300 K. *Filled diamonds* are for calcium apatites (Brunet et al. 1999; Comodi et al. 2001; Matsukage et al. 2004) while *squares* and *circles* for lead bromapatite and lead fluorapatite (Liu et al. 2008), respectively. *Filled square* and *circle* represent the best data-fitting result for lead fluorapatite and lead bromapatite, respectively

The pressure dependence of the *a*-axis can be represented by the regression equation $a = 10.054(5) - 0.0547(14)P + 0.00129(8)P^2$ and that of the *c*-axis by $c = 7.349(5) - 0.0295(15)P + 0.00085(9)P^2$, with *a* and *c* in Å and *P* in GPa. Similar to the unit-cell parameters of lead fluorapatite, the unit-cell parameters of lead bromapatite have a non-linear dependence on pressure over the investigated pressure range. In contrast, those of calcium fluorapatite were reported to have a linear dependence on pressure (Comodi et al. 2001; Matsukage et al. 2004). A careful examination of Fig. 4 shows that the data collected at pressures above 18 GPa deviate slightly from the trend defined by the lower pressure data. This phenomenon is likely due to the loss of the hydrostatic condition within the diamond-anvil cell caused by solidification of the pressure media, and is more clearly manifested by the plot of *a*/*c* versus *P* (Fig. 5). In contrast to the *a*/*c* ratio of lead fluorapatite, the *a*/*c* ratio of lead bromapatite over the investigated pressure range is manifestly dependent to pressure [$(a/c) = -0.00175(5)P + 1.3675(4)$], clearly indicating that lead bromapatite is elastically anisotropic (Table 6; Fig. 5). The systematic decrease in *a*/*c* is readily associated with the accommodation of the large Br anion in the apatite channel. The anomalous lateral displacements of structural elements (particularly of Pb2 and the PO_4 tetrahedron) away from the *c*-axis anticipate that lead bromapatite will be elastically weaker in the (001) plane than along the *c*-axis. Compressional anisotropy, albeit weak, has also been observed for fluorapatite (Sha et al. 1994; Brunet et al. 1999; Comodi et al. 2001; Matsukage et al. 2004).

The *P*–*V* data of lead bromapatite are compared with the *P*–*V* data of lead fluorapatite from Liu et al. (2008) in Fig. 6. Clearly, these two lead apatites have very similar bulk compressibilities. In addition, Fig. 6 indicates that the elastic behaviour of lead bromapatite is fully reversible after compression to 20.7 GPa.

In order to determine the elastic parameters, the *P*–*V* data have been fitted to the third-order Birch-Murnaghan equation of state (BM-EoS; Birch 1947) by a least-squares method:

$$P = 3K_T f_E(1+2f_E)^{\frac{5}{2}}\left[1+\frac{3}{2}\left(K_T'-4\right)f_E\right]$$

where *P* is the pressure, K_T the isothermal bulk modulus, K_T' the first pressure derivative of K_T, and f_E the Eulerian definition of finite strain, which is $[(V_0/V)^{2/3} - 1]/2$, respectively. In the Eulerian definition of finite strain, V_0 is the volume at zero pressure whereas *V* is the volume at high pressure. As illustrated in Figs. 4, 5, 6, the two datum points collected at 18.7 and 20.7 GPa significantly deviate away from the trends defined by other datum points, so that they were excluded from the calculation of the bulk modulus. Our calculation with the data collected below 18 GPa suggests $K_T = 63.8(21)$ and $V_0 = 645.0(9)$ as K_T' is set as 4, or $K_T = 48.3(10)$, $K_T' = 11.2(6)$ and $V_0 = 646.1(2)$. Since the data collected at pressures above 10 GPa were potentially affected by the inhomogeneous stress in the diamond-anvil cell due to the solidification of the pressure media at about 10 GPa, we also tried our calculation with those data gathered at pressures below 10 GPa. When K_T' is set as 4, the derived isothermal bulk modulus (K_T) of lead bromapatite is 60.8(11) GPa whereas the zero-pressure volume is 645.6(5) $Å^3$. If K_T' is not fixed, the results of our best data-fitting are $K_T = 49.8(16)$ GPa, $K_T' = 10.1(10)$ and $V_0 = 646.0(2)$ $Å^3$. In comparison to lead fluorapatite (Liu et al. 2008), therefore, lead bromapatite has a smaller isothermal bulk modulus (~12% smaller when K_T' is set as 4). Since the isothermal bulk moduli of calcium hydroxylapatite, calcium fluorapatite and calcium chlorapatite vary only up to ~5% (Brunet et al. 1999; Comodi et al. 2001; Matsukage et al. 2004), it is of interest to investigate the compressional behaviour of calcium bromapatite. By fixing K_T' to different values and calculating K_T, a correlation analysis of K_T and K_T' was also carried out and the result is shown in Fig. 7 (with the *P*–*V* data collected at pressure less than 10 GPa only). Apparently, the isothermal bulk modulus of lead bromapatite is less dependent to K_T' than that of lead fluorapatite. The available equations of state for a selection of apatites are summarized in Table 7.

A linearized third-order BM-EoS was exploited to obtain the axial EoS parameters of lead bromapatite (Angel 2000). By linearization of the third-order BM-EoS through

Table 7 Bulk modulus and first pressure derivative of various apatites

Chemical formula	K_T (GPa)	K'_T	Data source
$Ca_{10}(PO_4)_6F_2$	93(4)[a]	5.8(18)	Comodi et al. (2001)
	97.8(1)	4	Comodi et al. (2001)
	91.6(1)	4	Matsukage et al. (2004)
	97.9(19)	4	Brunet et al. (1999)
$Ca_{10}(PO_4)_6Cl_2$	97.5(18)	4	Brunet et al. (1999)
$Ca_{10}(PO_4)_6(OH)_2$	93.1(42)	4	Brunet et al. (1999)
$(Na_{0.87}Ca_{9.13})[(CO_3)_{0.95}(PO_4)_{5.05}]CO_3$	84(1)	4	Liu et al. (2011)
	73(2)	7.0(6)	Liu et al. (2011)
$Pb_{10}(PO_4)_6F_2$	68.4(16)	4	Liu et al. (2008)
	54.3(18)	8.1(6)	Liu et al. (2008)
$Pb_{10}(PO_4)_6Br_2$	60.8(11)	4	This study
	49.8(16)	10.1(10)	This study

[a] Number in parentheses represents one standard deviation in the rightmost digit

the substitution of the cube of a lattice parameter (for instance a) for the volume, the value of "linear-K_T" can be obtained, which is essentially one-third of the inverse of the zero-pressure linear compressibility of that axis. Using the compression data collected at pressures less than 10 GPa, we obtained (with $K'_T(a)$ and $K'_T(c)$ fixed as 4): $a_0 = 10.061(2)$ and $K_T(a) = 56.6(8)$ GPa for the a-axis; $c_0 = 7.356(5)$ and $K_T(c) = 77.9(49)$ for the c-axis. The elastic anisotropy of lead bromapatite thus appears to be significant, with the a-axis much more compressible than the c-axis ($K_T(c)/K_T(a) = 1.376$). Similarly, we processed the data for lead fluorapatite collected at pressures less than 10 GPa in Liu et al. (2008), and obtained: $a_0 = 9.732(24)$ and $K_T(a) = 92.7(148)$ GPa for the a-axis; $c_0 = 7.264(5)$ and $K_T(c) = 72.6(24)$ for the c-axis. Apparently lead fluorapatite has a weaker elastic anisotropy, but with the c-axis more compressible than the a-axis ($K_T(c)/K_T(a) = 0.783$). With the replacement of F by Br, interesting, the principle axes of the strain ellipsoids of the lead apatites switch directions.

Acknowledgments We thank J. Hu for her help with the synchrotron powder X-ray diffraction experiment, G.C. Yau for her help with the conventional powder X-ray analysis, G. Shu for his help with the electron probe microanalysis (JEOL JXA8100), and M. Jennings for collecting the single-crystal X-ray reflection data. We thank Editor M. Matsui for his constructive comments and editorial handling. Two anonymous reviewers are thanked for their very thorough and detailed reviews. This investigation was financially supported by the Natural Sciences and Engineering Research Council of Canada, and by the NSF of China (Grant 40730314).

References

Angel RJ (2000) Equation of state. In: Hazen RM, Downs RT (eds) High-temperature and high-pressure crystal chemistry. Reviews in mineralogy and geochemistry, vol 41. Mineralogical Society of American, Chantilly, pp 35–60

Badraoui B, Bigi A, Debbabi M, Gazzano M, Roveri N, Thouvenot R (2001) X-ray powder diffraction and solid state NMR investigations in cadmium-lead hydroxyapatites. Eur J Inorg Chem 2001:1261–1267

Badraoui B, Aissa A, Bigi A, Debbabi M, Gazzano M (2006) Structural investigations of lead-strontium fluoroapatites. J Solid State Chem 179:3065–3072

Bhatnaga VM (1971) Lead bromapatite, $Pb_{10}(PO_4)_6Br_2$. Inorg Nucl Chem Lett 7:231–232

Bigi A, Ripamonti A, Brückner S, Gazzano M, Roveri N, Thomas SA (1989) Structure refinements of lead-substituted calcium hydroxyapatite by X-ray powder fitting. Acta Crystallogr B45:247–251

Birch F (1947) Finite elastic strain of cubic crystals. Phys Rev 71:809–924

Boujrhal FZ, Hlil EK, Cherkaoui El Moursli R (2004) Study of apatite behaviour in the presence of the radionuclides U and Rn and local modification of their crystalline and electronic structure. Radiat Phys chem 69:1–6

Brückner S, Lusvardi G, Menabue L, Saladini M (1995) Crystal structure of lead hydroxyapatite from powder X-ray diffraction data. Inorg Chim Acta 236:209–212

Bruker-Nonius (1997) COLLECT software. Bruker-Nonius, Delft

Brunet F, Allan DR, Redfern SAT, Angel RJ, Miletich R, Reichmann HJ, Sergent J, Hanfland M (1999) Compressibility and thermal expansivity of synthetic apatites, $Ca_5(PO_4)_3X$ with X = OH, F and Cl. Eur J Mineral 11:1023–1035

Comodi P, Liu Y, Zanazzi PF, Montagnoli M (2001) Structural and vibrational behaviour of fluorapatite with pressure. Part I: In situ single-crystal X-ray diffraction investigation. Phys Chem Mineral 28:219–224

Condrate RA, Cornilsen BC, Dykes E (1975) Raman-spectrum of calcium bromapatite. Appl Spectros 29:526–527

Coppens P (1977) LINEX77. State University of New York, Buffalo

Cruz FJAL, Minas da Piedade ME, Calado JCG (2005a) Standard molar enthalpies of formation of hydroxyl-, chlor-, and bromapatite. J Chem Thermodyn 37:1061–1070

Cruz FJAL, Canongia Lopes JN, Calado JCG, Minas da Piedade ME (2005b) A molecular dynamics study of the thermodynamic properties of calcium apatites. 1. Hexagonal phases. J Phys Chem 109:24473–24479

Dykes E (1974) Preparation and characterization of calcium bromapatite. Mater Res Bull 9:1227–1236

Elliott JC, Kykes E, Mackie PE (1981) Structure of bromapatite and its radius of the bromide ion. Acta Crystallogr B 37:435–438

Filiberto J, Treiman AH (2009) Martian magmas contained abundant chlorine, but little water. Geology 37:1087–1090

Fleet ME (2009) Infrared spectra of carbonate apatites: *v*2-Region bands. Biomaterials 30:1473–1481

Fleet ME, Liu X (2007a) Hydrogen-carbonate ion in synthetic high-pressure apatite. Am Mineral 92:1764–1767

Fleet ME, Liu X (2007b) Coupled substitution of type A and B carbonate in sodium-bearing apatite. Biomaterials 28:916–926

Fleet ME, Liu X (2008a) Accommodation of the carbonate ion in fluorapatite synthesized at high pressure. Am Mineral 93:1460–1469

Fleet ME, Liu X (2008b) Type A-B carbonate chlorapatite synthesized at high pressure. J Solid State Chem 181:2494–2500

Fleet ME, Liu X, Shieh SR (2010) Structural change in lead fluorapatite at high pressure. Phys Chem Mineral 37:1–9

Hamilton WC (1965) Significance tests on the crystallographic R factor. Acta Crystallogr 18:502–510

Hammersley J (1996) Fit2D report. Europe Synchrotron Radiation Facility, Grenoble

Hughes JM, Rakovan J (2002) The crystal structure of apatite, $Ca_5(PO_4)3(F, OH, Cl)$. In: Kohn MJ, Rakovan J, Hughes JM (eds) Phosphates. Reviews in mineralogy and geochemistry, vol 48. Mineralogical Society of America, Chantilly, pp 1–12

Hughes JM, Cameron M, Crowley KD (1989) Structural variations in natural F, OH, and Cl apatites. Am Mineral 74:870–876

Ibers JA, Hamilton WC (eds) (1974) International tables for X-ray crystallography, vol IV. Kynoch Press, Birmingham

Kaluderovic T, Dudukovic A, Raicevic S (2001) Remediation of environment contaminated by lead using synthetic and natural apatites. Chem Ind 55:114–119

Kim JY, Fenton RR, Hunter BA, Kennedy BJ (2000) Powder diffraction studies of synthetic calcium and lead apatites. Aust J Chem 53:679–686

Krivovichev SV, Burns PC (2003) Crystal chemistry of lead oxide phosphates: crystal structures of $Pb_4O(PO_4)_2$, $Pb_8O_5(PO_4)_2$ and $Pb_{10}(PO_4)_6O$. Zeit Kristallogr 218:357–365

Liu X, Fleet ME (2009) Phase relations of nahcolite and trona at high P-T conditions. J Mineral Petrol Sci 104:25–36

Liu X, Shieh SR, Fleet ME, Akhmetov A (2008) High-pressure study on lead fluorapatite. Am Mineral 93:1581–1584

Liu X, Shieh SR, Fleet ME, Zhang L, He Q (2011) Equation of state of carbonated hydroxyapatite at ambient temperature up to 10 GPa: significance of carbonate. Am Mineral 95, doi:10.2138/am.2010.3535

Lodders K, Fegley B Jr (1998) The Planetary Scientist's companion. Oxford University Press, Oxford

Ma QY, Traina SJ, Logan TJ, Ryan JA (1993) In situ lead immobilization by apatite. Environ Sci Technol 27:1803–1810

Mao HK, Bell PM, Shaner JW, Steinberg DJ (1978) Specific volume measurements of Cu, Mo, Pt, and Au and calibration of ruby R1 fluorescence pressure gauge for 0.006 to 1 Mbar. J Appl Phys 49:3276–3283

Matsukage KN, Ono S, Kawamoto T, Kikegawa T (2004) The compressibility of a natural apatite. Phys Chem Mineral 31:580–584

Nriagu JO (1973) Lead orthophosphates-III. Stabilities of fluoropyromorphite and bromopyromorphite at 25°C. Geochim Cosmochim Acta 37:1735–1743

Nriagu JO (1984) Formation and stability of heavy metal phosphates in soils and sediments. In: Nriagu JO, Moore PB (eds) Phosphate minerals. Springer, New York, pp 318–329

O'Reilly SY, Griffin WL (2000) Apatite in the mantle: implications for metasomatic processes and high heat production in Phanerozoic mantle. Lithos 53:217–232

Pan Y, Dong P (2003) Bromine in scapolite group minerals and sodalite: XRF microprobe analysis, exchange experiments, and application to skarn deposits. Can Mineral 41:529–540

Pan Y, Fleet ME (2002) Compositions of the apatite-group minerals: substitution mechanisms and controlling factors. In: Kohn MJ, Rakovan J, Hughes JM (eds) Phosphates. Reviews in mineralogy and geochemistry, vol 48. Mineralogical Society of America, Chantilly, pp 13–49

Peters NJ, Davidson CM, Britton A, Robertson SJ (1999) The Nature of corrosion products in lead pipes used to supply drinking water to the City of Glasgow, Scotland, UK. Fresenius J Anal Chem 363:562–565

Podsiadlo H (1990) Polymorphic transitions in the binary system of lead fluorapatite $[Pb_{10}(PO_4)_6F_2]$-calcium fluorapatite $[Ca_{10}(PO_4)_6F_2]$. J Therm Anal Calorim 36:569–575

Rulis P, Ouyang L, Ching WY (2004) Electronic structure and bonding in calcium apatite crystals: hydroxyapatite, fluorapatite, chlorapatite, and bromapatite. Phys Rev B 70:155104

Sha MC, Li Z, Bradt RC (1994) Single-crystal elastic constants of fluorapatite, $Ca_5F(PO_4)_3$. J Appl Phys 75:7784–7787

Shannon RD (1976) Revised effective ionic radii and systematic studies of interatomic distances in halides and chalcogenides. Acta Crystallogr A32:751–767

Sudarsanan K, Mackie PE, Young RA (1972) Comparison of synthetic and mineral fluorapatite, $Ca_5(PO_4)_3F$, in crystallographic detail. Mater Res Bull 7:1331–1338

Suzuki T, Ishigaki K, Miyake M (1984) Synthetic hydroxyapatites as inorganic cation exchangers. J Chem Soc Faraday Trans I 80:3157–3165

Walters LJ Jr, Luth WC (1969) Unit-cell dimensions, optical properties, halogen concentrations in several natural apatites. Am Mineral 54:156–162

White TJ, Dong Z (2003) Structural derivation and crystal chemistry of apatites. Acta Crystallogr B 59:1–16

White TJ, Ferraris C, Kim J, Madhavi S (2005) Apatite-an adaptive framework structure. In: Ferraris G, Merlino S (eds) Micro- and meso-porous mineral phases. Reviews in mineralogy and geochemistry, vol 57. Mineralogical Society of America, Washington DC, pp 307–373